ACS APPLIED MATERIALS & INTERFACES

Research Article

www.acsami.org

Influence of Annealing Temperature of WO_3 in Photoelectrochemical Conversion and Energy Storage for Water Splitting

Charlene Ng, Yun Hau Ng,* Akihide Iwase,[†] and Rose Amal*

ARC Centre of Excellence for Functional Nanomaterials, School of Chemical Engineering, The University of New South Wales, Sydney New South Wales 2052, Australia

ABSTRACT: The current work demonstrates the importance of WO_3 crystallinity in governing both photoenergy conversion efficiency and storage capacity of the flower structured WO_3 electrode. The degree of crystallinity of the WO_3 electrodes was varied by altering the calcination temperature from 200 to 600 °C. For the self-photochargeability phenomenon, the prevailing flexibility of the short-range order structure at low calcination temperature of 200 °C favors the intercalation of the positive cations, enabling more photoexcited electrons to be stored within WO_3 framework. This leads to a larger amount of stored charges that can be discharged in an on-demand manner under the absence of irradiation for H_2 generation. The stability of the electrodes calcined at 200 °C, however, is compromised because of the structural instability caused by the abundance insertion of cations. On the other hand, films that were calcined at 400 °C displayed the highest stability toward both intercalation of the cations and photoelectrochemical water splitting performance. Although crystallinity of WO_3 was furthered improved at 600 °C heat treatment, the worsened contact between the WO_3 platelets and the conducting substrate as induced by the significant sintering has been more detrimental toward the charge transport.

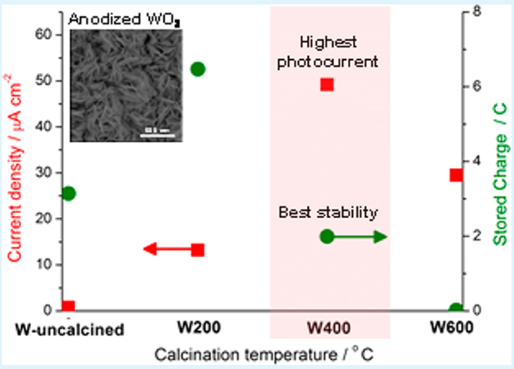

KEYWORDS: *crystallinity, hydrogen generation, photoelectrochemical water splitting, self-photorecharge, tungsten oxide*

■ INTRODUCTION

Tungsten oxide (WO_3) has been widely studied as a photoanode material in photoelectrochemical (PEC) systems, due to its high stability in aqueous solution and proper energy band gap (<3.0 eV) for visible-light utilization.[1−4] Despite there being a considerable amount of research on photoexcited WO_3,[5−7] the research focused mainly on understanding and optimizing photogenerated charges under continuous illumination. Recently, we have reported a self-photochargeability phenomenon that extends the functionality of the WO_3 photoelectrodes without continuous irradiation, allowing photoexcited charges to be stored and utilized for H_2 generation in the absence of light.[8,9] The self-photorechargeability phenomenon is proposed to be related to the intercalation of alkali cations into the WO_3 structure and thereby trapping the photoexcited electrons that can be discharged subsequently in dark. Unlike the typical WO_3 photoelectrode system which functions solely under the presence of illumination, the self-photorechargeability property of WO_3 photoelectrode allows it to generate H_2 under dark condition by utilizing the stored photoexcited electrons. Overall, the intriguing self-photorechargeability phenomenon serves as the ability toward energy harvesting, conversion and storage by the use of a single material. Further study toward the optimization of the charge storage property was investigated by varying the system variables such as concentration of electrolyte and time for the photocharging process. We found that the charge storage ability and reversibility performance of the electrode were highly dependent on the concentration of alkali cations in the electrolyte solution.[9] However, from these previous studies, it is still unclear what material properties of WO_3 govern the self-photorechargeability property.

The crystallinity of films has been widely reported to have an impact on the storage ability of WO_3 when combined with TiO_2 and in electrochromic applications.[10,11] Cao et al. investigated the TiO_2−WO_3 composite and found that the storage capability of WO_3 was affected by the crystal structure and improved with low degree of crystallinity.[10] Higashimoto et al. also reported similar trend in the TiO_2/WO_3 composite, where amorphous WO_3 exhibited larger discharging capacity than the crystalline WO_3.[11] Electrochromic applications involving analogous intercalation of alkali cations into WO_3 structure also demonstrated difference in electrochromic performance associated to its level of crystallinity.[12−16] Generally, amorphous WO_3 are more suitable in the construction of electrochromic devices, because of the faster response time related to the rapid movement of cations through the loose structure of amorphous WO_3. From these studies, it was evident that the level of crystallization had a significant impact on the degree of cations intercalation related

Received: March 27, 2013
Accepted: May 23, 2013
Published: June 3, 2013

dx.doi.org/10.1021/am401112q | *ACS Appl. Mater. Interfaces* 2013, 5, 5269−5275

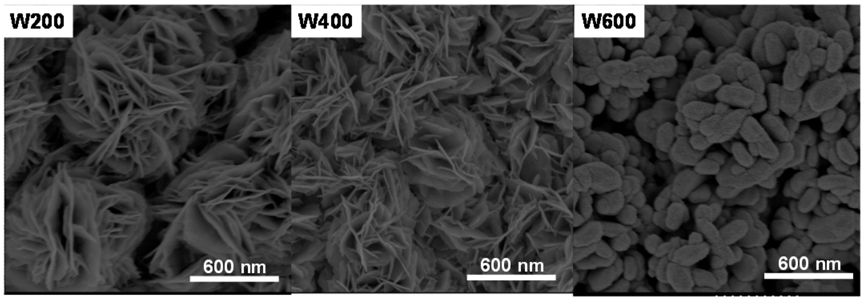

Figure 1. SEM images of flower-structured (F) WO_3 films at different calcination temperature (200, 400, and 600 °C).

to the charge storage property of WO_3. Therefore, understanding the intricate relationships between material properties particularly on the crystallinity property of WO_3 and the self-photorecharge property is crucial in order to optimize the charge storage capacity.

On the other hand, it is well-known that the level of crystallization and annealing temperature also influences the energy conversion and photoelectrochemical water splitting performance, as the number of grain boundaries and recombination centers associated with the degree of crystallinity will influence the charge separation and electron transport pathway of the material. Ahn et al.[17] investigated the photoelectrochemical responses of WO_3 films as a function of the calcination temperature and found that the crystallinity of the WO_3 films improves and light absorption is enhanced with increasing annealing temperature. However, the films annealed at 500 °C displayed the best photoelectrochemical property, whereas films annealed at 600 °C reflected a decreased performance, indicating the existence of an optimum annealing temperature. Currently, there is no study directed toward the understanding between crystallinity and the energy conversion efficiency along with the storage capacity of the flower-structured WO_3 synthesized by the anodization technique. Therefore, it is of immense importance to understand this relationship in order to optimize the H_2 generation ability of the unique flower-structured WO_3.

In this work, the influence of annealing temperature in optimizing both self-photorechargeability performance and PEC water splitting will be studied on the flower-structured WO_3 films, found to be able to convert and store photoenergy in one material system. The morphology and degree of crystallinity of these flower-structured films are varied by altering the calcination temperature between 200 to 600 °C, and characterized by scanning electron microscopy (SEM) and X-ray diffraction (XRD). Furthermore, the amount of H_2 evolved during the illumination of the WO_3 films and after the light is turned off will be measured to evaluate its solar energy conversion efficiency and self-photocharging ability.

1. EXPERIMENTAL SECTION

1.1. Synthesis of WO_3 Films.

Tungsten (W) foils (Alfa Aesar, 99.95%, 0.05 mm thick) were anodized in 120 mL of electrolyte solution consisting of 1 M of sulphuric acid (H_2SO_4, Univar, 98%) and 0.5 wt % sodium fluoride (NaF, Analar, 99%). Prior to the electrochemical anodization process, the tungsten foils were degreased by sonicating in acetone and followed by deionized water. The samples were then contacted with a Cu spring and pressed against an O-ring in an anodization cell, leaving 4.15 cm^2 exposed to the electrolyte solution. The anodization cell consists of a two-electrode configuration with a platinum foil as the counter electrode (cathode) and the tungsten foil as the working electrode (anode); the distance between the cathode and the anode was kept constantly at 2 cm. All experiments were performed in static conditions. For anodization the voltage was held at 50 V for 60 min. The anodized samples were then properly washed with deionized water and air-dried. Subsequently, thermal treatment of the WO_3 films was carried out at 400 °C for 4 h with a ramping rate of 2 °C/min in air environment. The samples were then allowed to cool down by natural convection in the furnace back to ambient condition. The samples are abbreviated by W and calcination temperature (uncalcined, 200, 400, and 600) as follows: W-uncalcined indicate flower-structured and WX00 indicate flower-structured films that were annealed at *X*00 °C (*X* = 2, 4, 6).

1.2. Material Characterization.

A scanning electron microscope (SEM, Hitachi S900, operating accelerating voltage of 5 kV) was used to analyze the morphology of the WO_3 nanostructures. XRD measurements were collected at room temperature using Cu Kα radiation (λ = 1.54 Å) with a potential of 40 kV and a current of 30 mA (Philips PW1830). Diffuse reflectance ultraviolet and visible (DRUV−vis) spectra of the films were recorded in a range of 200−800 nm to investigate the light harvesting properties of WO_3 thin films using a UV−vis spectrophotometer (Cary 5 UV−vis−NIR).

1.3. Photoelectrochemical Measurements.

Photoelectrochemical measurements of the samples were taken in 0.1 or 0.5 M electrolyte solution at room temperature using Autolab potentiostat/galvanostat (model PGSTAT302N) at 1.0 V in a two-electrode configuration with platinum as the counter electrode and reference electrode, WO_3 film as the working electrode. Potassium sulfate (K_2SO_4, Sigma Aldrich, ≥99%) and sulphuric acid (H_2SO_4, Univar, 98%) were utilized as the respective electrolyte solution for self-photorechargeability phenomenon and PEC water splitting application. Argon gas was bubbled in the system for 1 h prior to the measurements to remove any dissolved oxygen in the cell. For visible-light illumination, a cutoff filter was used to obtain light of wavelength $\lambda \geq 420$ nm from a 300 W Xe lamp (Oriel). IPCE measurements were taken at 1.0 V in H_2SO_4 electrolyte solution using Newport integrated monochromator to generate selected wavelengths with IPCE calculated as follows.

$$[\mathrm{IPCE}/\%] = 1240 \times [\text{photocurrent density}/\mu\mathrm{A\,cm^{-2}}] \\ /([\text{wavelength}/\mathrm{nm}] \times [\text{photo flux}/\mathrm{W\,m^{-2}}])$$

1.4. Photoelectrochemical Water Splitting.

PEC water splitting experiments were carried out by applying external bias of 1.0 V in a two-electrode cell with WO_3 as the working electrode and Pt as the counter electrode placed separately in each compartment with both electrodes being immersed in H_2SO_4 or K_2SO_4 electrolyte solution. Argon gas was being employed as the main carrier gas in the whole system. The light sources employed are 300 W Xe lamp with a cutoff filter used to obtain visible light of wavelength $\lambda \geq 420$ nm and a solar simulator AM 1.5 G. The evolved H_2 and O_2 were determined with gas chromatography (Shimadzu, GC-8A detector (TCD)).

Solar energy conversion efficiency was calculated as follows.[18]

$$[\text{solar energy conversion efficiency}/\%] = 100 \times [\Delta G^0(\mathrm{H_2O})/\mathrm{J\,mol^{-1}}] \times (1.23 - E_{\text{apply}}/1.23) \times [\text{rate of H}_2\text{ evolution}/\mathrm{mol\,h^{-1}}]/(3600 \times [\text{solar energy(AM1.5)}/\mathrm{W\,cm^{-2}}] \times [\text{dimension of electrode}/\mathrm{cm^2}])$$

2. RESULTS AND DISCUSSION

2.1. Morphology of WO_3 Films. Figure 1 depicts the morphology of the flower-structured WO_3 films at different calcination temperature: 200, 400, and 600 °C. The flower-structured samples are abbreviated by W and calcination temperature (uncalcined, 200, 400 and 600) as follows; W-uncalcined indicates the uncalcined films, while W200, W400, and W600 correspond to the films that were annealed at 200, 400, and 600 °C, respectively. The SEM images of the flower-structured films before heat treatment exhibit similar morphology as the films that are calcined at 200 °C (W200). Intertwined platelets with a thickness of 10−15 nm radiating in all directions that leads to a flower-like morphology is achieved under supersaturation condition. Preservation of the morphology is observed up to an annealing temperature of 400 °C (W400), where no significant change in the structure can be identified from the SEM images. After the films are calcined at 600 °C (W600), the platelets in the flower-structured WO_3 aggregated to form elongated particles. Apparent morphological changes in the film only occurred upon heat treatment at 600 °C (W600), whereby sintering of the structures arises to lower the surface free energy that leads to a decrease in the surface area.

2.2. Crystal Structure of WO_3 Films. XRD patterns of the flower-structured WO_3 films after annealing at 200 °C, 400 and 600 °C for 4 h are illustrated in Figure 2. XRD spectra revealed the presence of monoclinic $WO_3·2H_2O$ on the as-anodized film (W-uncalcined) with the highest peak indexed to (010) plane, while (200) and (020) peaks correspond to the monoclinic structure. The crystal structure of $WO_3·2H_2O$ is composed of H_2O molecules accommodated between the corner sharing $WO_5(H_2O)$ octahedral layers as interlayer crystal water with the octahedral layers bonded by hydrogen bonds between the O and H atoms in neighboring layers.[2,19,20] After calcination at 200 °C, no apparent peak but a broad hump observed at 25° suggesting the presence of short-range order WO_3 related to the intermediate transition from $WO_3·2H_2O$ to WO_3. The relatively low annealing temperature is insufficient for the rearrangement of the WO_6 octahedral and subsequent formation of crystalline structure, resulting in structure with short-range order. The monoclinic $WO_3·2H_2O$ is also shown to experience a loss of water after the heat treatment at 200 °C, as confirmed by the disappearance of strong intensity peak at 13.0° corresponding to (010) plane.

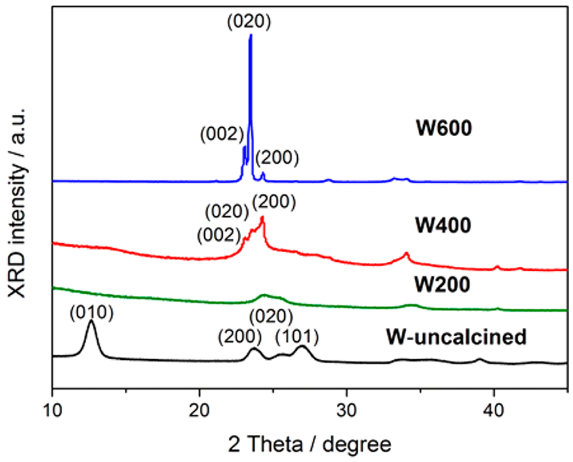

Figure 2. XRD patterns of flower-structured WO_3 films at different calcination temperature of 200, 400, and 600 °C.

At calcination temperature of 400 °C, the presence of three characteristic peaks at 23.1, 23.6, and 24.4° corresponding to (002), (020), and (200) planes confirmed the presence of monoclinic WO_3 on W400. The complete transformation of $WO_3·2H_2O$ to monoclinic WO_3 is further confirmed by the absence of diffraction peaks (010) indexed to layered crystallites. Monoclinic WO_3 has a distorted ReO_3 structure with corner-sharing distorted and tilted WO_6 octahedral connected to form a three-dimensional structure.[2] The existence of crystalline monoclinic WO_3 verified the adequate heat treatment required for the rearrangement of the WO_6 octahedral, where the hydrogen bonds are replaced by W−O−W bonds to form a three-dimensional network structure. It should be noted that the flower-structured morphology is maintained during the dehydration process with the resultant W400 taking on a similar structure as shown in Figure 1. Monoclinic WO_3 with a predominated preferred orientation toward (020) is similarly observed on the W600 films. Annealing at 600 °C led to further improvement in the crystallinity of the films as indicated by the strong increase in the intensity of the peaks and a decrease in the peak width on W600. However, the improvement in crystallinity of W600 is accompanied with a significant sintering of the WO_3 platelets as indicated in Figure 1, where the originally thin and perpendicularly formed WO_3 platelets have been sintered to relatively thick oval-shaped fused particles. Moreover, the peak of the (020) plane for W600 also indicates a preferential orientation of the WO_3 crystal faces in the [020] direction caused by the high calcination temperature, which is in accordance with the studies by Guo et al.[21] and Ye et al.[22]

2.3. Effect of Annealing Temperature on Self-Photorecharge and Storage Property. The charge storage ability of the flower-structured WO_3 films at different calcination temperature in 0.5 M K_2SO_4 is illustrated in Figure 3. All samples are photocharged under visible-light irradiation for 4 h and the stored charges are subsequently discharged under dark condition for 8 h. The charge storage ability is evaluated by the total amount of charge (coulomb) that is released during the discharging period. W200 displays the highest storage ability among all the samples and the amount of stored charge decreases with increasing calcination temperature from 200 to 600 °C. The relatively low storage ability of the W-uncalcined sample suggests that the H_2O molecules located between the layers of $WO_5(H_2O)$ octahedral occupied the possible storage sites that are available for the intercalation and storage of K^+ ions. On the other hand, the level of crystallization achieved at different calcination temperature plays a significant role in the storage behavior of these films. High storage ability reflects a corresponding high intercalation efficiency of the K^+ ions. At low calcination temperature condition (200 °C), the short-range order and disorder nature within the WO_3 framework introduces flexibility that promotes the mobility of K^+ ions and also creating more storage sites to accommodate the intercalation of the K^+ cations. Moreover, [W−O] polygonal

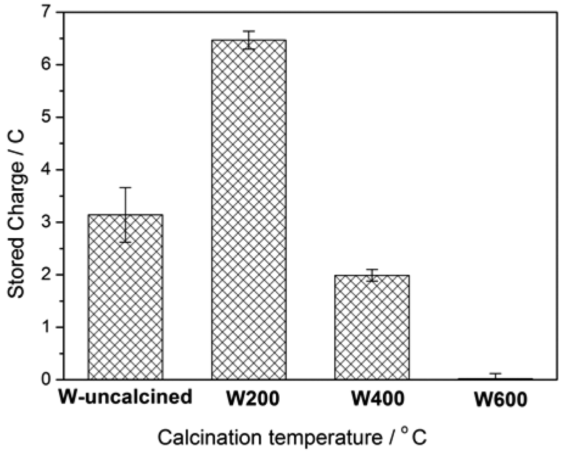

Figure 3. Amount of charge storage of flower-structured WO_3 films at different calcination temperature of 200, 400, and 600 °C. Applied potential, 1.0 V vs Pt; electrolyte, 0.5 M K_2SO_4 solution; light source, 300 W Xe lamp with cutoff filter ($\lambda \geq 420$ nm).

tunnels with large size and distorted structures channel formed by oxygen vacancy existed within the amorphous structure, giving rise to a comparatively loose structure for the movement of cations.[10] In contrast, W600 is less favorable for the intercalation of K^+ ions due to its densely packed structure, which would limit and obstruct the K^+ ions movement through the film.[12,23,24] The [W−O] polygonal tunnel structure also becomes small and compact with calcination, causing difficulty for the movement of the cations.[10]

Despite the high intercalation efficiency demonstrated by the uncalcined and 200 °C films, they are relatively unstable after the photocharge−discharge cycle. Detachment of the oxide layer from the electrode and residual blue coloration of the films can be observed after the reaction. The residual blue coloration is an indication of irreversibly trapped K^+ ions in the framework as confirmed in our previous work,[9] whereas the detached oxide layer implies a structural breakdown and low stability of the noncrystalline lattice toward K^+ insertion, as a result of the abundant insertion and slow diffusivity of K^+ ions.[25] On the other hand, W400 showed superior stability and insertion reversibility as compared to W200 after the photocharge−discharge cycle, despite the lower storage capacity.

The disappearance of the W200 flower-structured platelets after the cycle (Figure 4A) clearly reflects the detachment of the oxide layer from the W substrate, while W400 (Figure 4B) demonstrated high insertion reversibility with minimal changes observed on the SEM image after reaction. Comparing the XRD results in Figure 4C, apparent WO_3 peaks are present in W400 before and after the cycle, whereas the disappearance of the broad peak at approximately 25° for W200 indicates the loss of the oxide layer after the cycle. These observations suggest that there is a limit at which the K^+ ions can be reversibly inserted, as the slow diffusivity of K^+ and its electric charge will possibly create a mechanical strain on the WO_3 host.[26] The high concentration of inserted K^+ ions can also

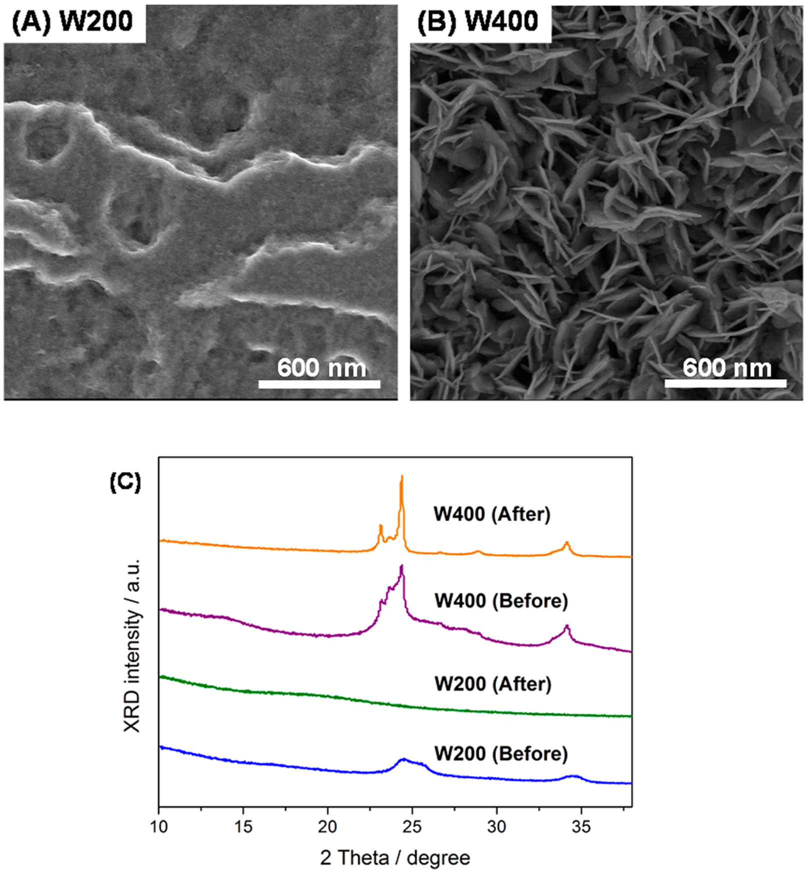

Figure 4. SEM images of the (A) W200 and (B) W400 after one charge−discharge cycle and (C) XRD spectra of the films before and after the charge−discharge cycle to illustrate the high reversibility of the W400 sample.

possibly cause a deformation on the host oxide because of a phase transition occurring within the films after the photo-charge−discharge cycle. Moreover, there are several defect states including W−O−H and W═O sites present in the amorphous WO_3, which may act as intercalated ion trapping sites.[13] Therefore, a balance between the intercalation capability and the insertion reversibility of the films has to be attained for the practical utilization of these WO_3 electrodes for simultaneous solar energy conversion and storage.

2.4. Effect of Annealing Temperature on PEC Water Splitting. The photocurrent−time measurements are also conducted on the films to investigate the PEC water splitting performance of the flower-structured WO_3 films (Figure 5) at different calcination temperatures. Our previous study[8] has proven 100% Faradaic efficiency in the current-to-hydrogen generation. The H_2 production performance in this current work using the identical system can be reflected by the photocurrent measurements. The generated photocurrent was recorded for a period of 3 h under visible-light irradiation (≥420 nm) in a two electrode setup with Pt as the counter electrode and 0.1 M H_2SO_4 as the electrolyte solution. Argon gas is bubbled through the system prior to the PEC measurements to remove any dissolved O_2, which otherwise would result in the reduction of oxygen rather than the production of H_2 as the dominant cathodic reaction.[27]

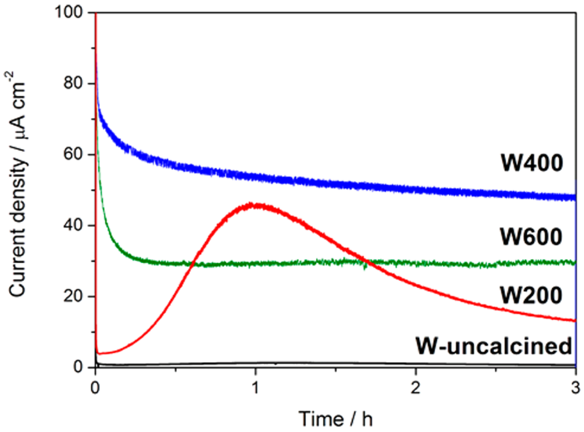

Figure 5. Photocurrent of the flower-structured WO_3 films at different calcination temperature of 200, 400, and 600 °C. Applied potential, 1.0 V vs Pt; electrolyte, 0.1 M H_2SO_4 solution; light source, 300 W Xe lamp with cutoff filter ($\lambda \geq 420$ nm).

W400 generates the highest photocurrent of 50 μA cm^{-2} among all the samples, while the insignificant photocurrent of 1.6 μA cm^{-2} is exhibited by the W-uncalcined sample (as-anodized $WO_3{\cdot}2H_2O$). The low photoresponse of the W-uncalcined sample arises as a result of poor crystallinity of the material that is reflected by the low peak intensity and peak broadening in the XRD pattern of W-uncalcined (Figure 2).[28] Significantly enhanced photocurrent exhibited by W400 and W600 suggests that the transformation to monoclinic WO_3 along with the loss of water molecules upon annealing improved the photoresponse of the flower-structured WO_3. The enhanced photocurrent with improved crystallinity can be attributed to the decreased number of recombination sites from the electronic structure.[17,29] However, despite W600 having the highest degree of crystallinity, it did not exhibit the highest photoelectrochemical performance. First, the sintering effect at high temperature of 600 °C resulted in larger elongated particles that give rise to a reduced effective surface area exposed to the electrolyte. The high crystallinity attained by these samples is traded-off by sintering of the nanostructures, resulting in a poorer performance. Second, the poor performance of W600 can be attributed to the difference in particle shape. The electrons excited on the surface of the W600 film need to migrate through the stacked and sintered particles of W600 (Figure 1) to the conducting substrate, resulting in higher recombination losses at the grain boundaries and recombination centers. In contrast, the flower-structured WO_3 results in almost vertically aligned platelets that facilitate the electron transport from the surface of the film to the conducting substrate.[28,30] More importantly, the high calcination temperature also results in poor attachment of the oxide layer (W600) on the W substrate as demonstrated by the ease of oxide removal in the form of powder after calcination. This observation can be caused by the high calcination temperature of 600 °C that induces interparticle rigidity, resulting in lower stability of the W600 film. The poor attachment of the oxide layer possibly affects the electron transport from the oxide layer to the conducting substrate, resulting in less electrons being transported to the cathode. Therefore, considerations into the various contributing factors such as structural stability, electron transport, and effective surface area have to been taken into account for the photocurrent performance of the materials.

In Figure 5, the current density of W200 increases gradually with time and decreases after the peak is reached within 1 h irradiation time. The current behavior is analogous to the self-photorechargeability phenomenon that were reported previously[8] and to be associated with the alkali cations (Na^+, Li^+, and K^+) present in the electrolyte during PEC measurements. No self-photorecharge ability is reported previously for W400 in the H_2SO_4 electrolyte because the small ionic radii of H^+ ions that are able to deintercalate from the WO_3 framework instantaneously. Interestingly, in the present study, a similar self-photorechargeability phenomenon is observed in the H_2SO_4 electrolyte where W200 are used as the working electrode. W200 is shown to exhibit a short-range order structure from the XRD spectra due to the absence of prominent diffraction peaks that can be indexed to crystalline WO_3. Hence, the analogous phenomenon in H_2SO_4 can be elucidated by the short-range order nature of the films that provides flexibility to the WO_3 framework to accommodate and possibly store the photoexcited electrons with a simultaneous intercalation of the H^+ ions. However, the W200 current increases initially and decreases after reaching the highest point. The development of the current in the first 1 h is proposed to be related to the reversible intercalation/deintercalation of the alkali cations during the photocharging process. In contrast, the decreasing current behavior after 1 h could be due to the trapped alkali cations that are being irreversibly intercalated into the WO_3 framework and occupied the available storage sites. The presence of these trapped alkali cations is verified by the residual blue coloration observed only on the W200 film after the PEC measurements. Similar blue coloration was also observed in our previous study,[9] where the presence of trapped alkali cations was confirmed. The existence of these trapped cations then results in a decreasing amount of storage sites that are available for the reversible intercalation/deintercalation of the cations, as reflected by the observed decreasing current behavior.

2.5. Optical Properties of W400. W400 demonstrate moderate crystallinity and represented a good compromise between the self-photocharge property and the stability of the metal oxide. Furthermore, it also featured the highest photocurrent performance for the PEC water splitting application as lower and higher calcination temperature has a detrimental effect on its photocurrent performance. Therefore, further investigations from this point onward will be focusing on the W400 sample. The optical behavior of the W400 film investigated by the UV−vis absorbance spectra and the incident proton to current efficiency (IPCE) measurements are illustrated in Figure 6. The absorption edge is positioned at 430 nm corresponding to band gap energy of 2.88 eV, illustrating its ability to respond under visible-light irradiation. The IPCE measured in 0.1 M H_2SO_4 at an applied voltage of 1.0 V versus Ag/AgCl also matches well with the absorption edge of the UV−vis spectrum confirms the generation of photocurrent originates from the excitation of the band gap of WO_3. The relatively moderate IPCE performance of the material is due to the moderate crystallinity of W400 and the low absorption coefficient of the thin platelets (20 nm thickness), resulting in the platelets of the flower-structure appearing to be transparent to the wavelength.

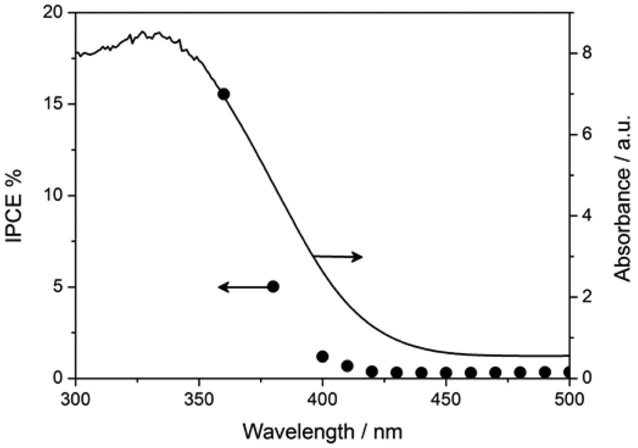

Figure 6. UV−vis absorbance spectrum and IPCE of the W400 film to illustrate the visible-light activity of the material (electrolyte, 0.1 M H_2SO_4; potential, 1.0 V vs Ag/AgCl; light source, 300 W Xe lamp with cutoff filters).

2.6. Hydrogen Generation Measurements. Figure 7A illustrates the current and corresponding rate of hydrogen gas (H_2) evolution under similar condition in 0.1 M H_2SO_4 electrolyte under visible-light irradiation (cutoff filter ≥420 nm). The performed PEC water splitting reaction utilizes light energy to drive the thermodynamically uphill conversion of water to its constituent elements as the reaction is assisted by a small applied voltage of 1.0 V that is smaller than 1.23 V. The anodic photocurrent is observed to be approximately 0.2 mA, whereas the H_2 gas evolution rate remains approximately 4 μmol h^{-1} within 4 h of visible-light illumination. PEC water splitting is also conducted using a solar simulator (AM 1.5) in Figure 7A and similar H_2 gas evolution rate of approximately 4 μmol h^{-1} is also evolved at 1.0 V vs Pt applied bias under the simulated solar irradiation. The solar energy conversion efficiency is estimated to be 0.0106% from the H_2 evolution rate, indicating that solar water splitting is successfully achieved by the WO_3 electrode. It is important to note that the higher photocurrent observed under visible-light illumination as compared to the simulated solar irradiation is attributed to the higher light intensity of the Xenon lamp used.

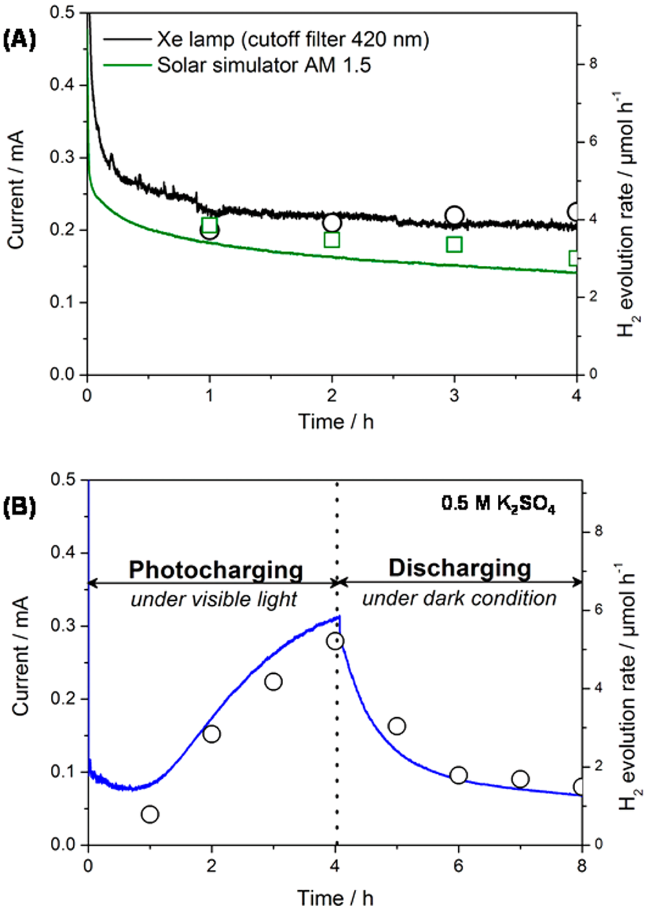

Figure 7. Anodic photocurrent of W400 (line) and the rate of H_2 evolution (symbols) for (A) PEC water splitting and (B) self-photorechargeability phenomenon using W400 electrode under visible-light irradiation. Applied potential, 1.0 V vs Pt; electrolyte, 0.1 M H_2SO_4 and K_2SO_4 solution; light source, 300 W Xe lamp with cutoff filter ($\lambda \geq 420$ nm) (○) and solar simulator AM 1.5 (□).

Figure 7B shows the W400 current generation and corresponding rate of hydrogen gas (H_2) evolution in the PEC water splitting reaction during photocharging under visible-light irradiation (cutoff filter ≥420 nm) and discharging under dark condition in 0.5 M K_2SO_4 electrolyte. During the 4 h photocharging process, the current and H_2 gas evolution rate increases with time signifying the continuous charge storage process in K_2SO_4 under visible-light irradiation. When the light is turned off after 4 h of irradiation, significant discharge current and H_2 gas evolution observed in the K_2SO_4 electrolyte confirms the ability to photocharge the WO_3 electrode and supply the stored electrons in dark to the water splitting reaction to form H_2. The calculated H_2 evolution agreed well with the measured photocurrent activity as shown in Figure 7A, indicating close to 100% current-to-hydrogen efficiency and anodic photocurrent was almost consumed for the production of H_2. The absence of observed oxygen (O_2) evolution in this experiment can be explained by the relatively low photocurrent that leads to minute production rate of O_2 gas that is beyond the detection limit of the gas chromatography. O_2 evolution has been detected in a separate experiment under UV irradiation that generates higher photocurrent as compared to visible-light irradiation. The absence of O_2 detection can also be elucidated by the high solubility of O_2 in water (1.4 μmol/mL under 1 atm at 20 °C)[31] and the photoadsorption of O_2 molecules onto the surface of the WO_3 electrode. Moreover, WO_3 is also recognized as an oxygen-evolving photocatalyst and has been reported previously by various authors to exhibit O_2 evolution activity under visible-light irradiation.[32−3435]

3. CONCLUSIONS

The annealing temperature and crystallinity of the anodized WO_3 materials was found to be the critical factor for self-photochargeability and PEC water splitting. For the self-photochargeability phenomenon, the charge storage ability increases with decreasing calcination temperature with the films that exhibit short-range order (W200) displayed the highest storage capability. The short-range order nature within the WO_3 framework introduces flexibility that promotes the mobility of K^+ ions and also creating more storage sites to accommodate the intercalation of the K^+ cations. However, the abundance insertion of K^+ ions into the W200 films also generated strain within the electrode and reduced the cyclic reversibility of these films. Therefore, film (W400) with moderate crystallinity that compromised between the charge storage ability and cyclic reversibility of the electrode was the best candidate material for self-photorecharge property. For PEC water splitting application, despite W600 having the highest crystallinity among all the films, W400 exhibited the highest PEC water splitting performance. This is due to the difference in particle shape and the sintering effect at high calcination temperature that decreases the effective surface area of the films and worsens the contact between WO_3 and charge collecting electrode. Hence, the relatively good crystallinity of W400 and the preservation of morphology and high effective surface area contributed to its highest performance in PEC water splitting application. Lastly, hydrogen gas evolution was detected using the W400 film as the photoanode for both applications, depicting the ability of this material to convert and store solar energy in one system.

■ AUTHOR INFORMATION

Corresponding Author

*E-mail: yh.ng@unsw.edu.au (Y.H.N.); r.amal@unsw.edu.au (R.A.).

Present Address

[†]A.I. is currently at Department of Applied Chemistry, Tokyo University of Science, 1−3 Kagurazaka Shinjuku-ku, Tokyo 162-8601

Notes

The authors declare no competing financial interest.

■ ACKNOWLEDGMENTS

The work was financially supported by Australian Research Council Discovery Project (DP110101638). The authors also acknowledge the UNSW Mark Wainwright Analytical Centre for access to the facility in obtaining SEM and XRD results.

■ REFERENCES

(1) Su, J.; Feng, X.; Sloppy, J. D.; Guo, L.; Grimes, C. A. *Nano Lett.* **2011**, *11*, 203−208.
(2) Chen, D.; Gao, L.; Yasumori, A.; Kuroda, K.; Sugahara, Y. *Small* **2008**, *4*, 1813−1822.
(3) Naseri, N.; Kim, H.; Choi, W.; Moshfegh, A. Z. *Int. J. Hydrogen Energy* **2013**, *38*, 2117−2125.
(4) Kim, J.; Lee, C. W.; Choi, W. *Environ. Sci. Technol.* **2010**, *44*, 6849−6854.
(5) Wang, H.; Lindgren, T.; He, J.; Hagfeldt, A.; Lindquist, S. *J Phys Chem B* **2000**, *104*, 5686−5696.
(6) Sadale, S. B.; Chaqour, S. M.; Gorochov, O.; Neumann-Spallart, M. *Mater. Res. Bull.* **2008**, *43*, 1472−1479.
(7) Yagi, M.; Maruyama, S.; Sone, K.; Nagai, K.; Norimatsu, T. *J. Solid State Chem.* **2008**, *181*, 175−182.
(8) Ng, C.; Ng, Y. H.; Iwase, A.; Amal, R. *Phys. Chem. Chem. Phys.* **2011**, *13*, 13421−13426.
(9) Ng, C.; Iwase, A.; Ng, Y. H.; Amal, R. *ChemSusChem* **2013**, *6*, 291−298.
(10) Cao, L.; Yuan, J.; Chen, M.; Shangguan, W. *J. Environ. Sci.* **2010**, *22*, 454−459.
(11) Higashimoto, S.; Kitahata, N.; Mori, K.; Azuma, M. *Catal. Lett.* **2005**, *101*, 49−51.
(12) Patel, K. J.; Panchal, C. J.; Desai, M. S.; Mehta, P. K. *Mater. Chem. Phys.* **2010**, *124*, 884−890.
(13) Bathe, S. R.; Patil, P. S. *Smart Mater. Struct.* **2009**, *18*, 025004−025011.
(14) Zhang, J.; Benson, D. K.; Tracy, C. E.; Deb, S. K.; Czanderna, A. W.; Bechinger, C. *J. Electrochem. Soc.* **1997**, *144*, 2022−2026.
(15) Agrawal, A.; Cronin, J. P.; Zhang, R. *Solar Energy Mater. Solar Cells* **1993**, *31*, 9−21.
(16) Lee, S.; Seong, M. J.; Cheong, H. M.; Ozkan, E.; Tracy, E. C.; Deb, S. K. *Solid State Ionics* **2003**, *156*, 447−452.
(17) Ahn, K.; Lee, S.; Dillon, A. C.; Tracy, C. E.; Pitts, R. *J. Appl. Phys.* **2008**, *101*, 093524.1−093524.4.
(18) Iwase, A.; Kudo, A. *J. Mater.Chem.* **2010**, *20*, 7536−7542.
(19) Tanaka, Y.; Miyayama, M.; Hibino, M.; Kudo, T. *Solid State Ionics* **2004**, *171*, 33−39.
(20) Li, Y. M.; Hibino, M.; Miyayania, M.; Kudo, T. *Solid State Ionics* **2000**, *134*, 271−279.
(21) Guo, Y.; Quan, X.; Lu, N.; Zhao, H.; Chen, S. *Environ. Sci. Technol.* **2007**, *41*, 4422−4427.
(22) Huang, Y.; Liu, Y. Y.; Li, W. Z.; Chen, Q. Y. *Acta Phys. Chim. Sin.* **2012**, *28*, 865−869.
(23) Baeck, S. H.; Choi, K. S.; Jaramillo, T. F.; Stucky, G. D.; McFarland, E. W. *Adv. Mater.* **2003**, *15*, 1269−1273.
(24) Lu, Y.; Hu, C. *J. Alloys Compd.* **2008**, *449*, 389−392.
(25) Brezesinski, T.; Rohlfing, D. F.; Sallard, S.; Antonietti, M.; Smarsly, B. M. *Small* **2006**, *2*, 1203−1211.
(26) Dini, D.; Decker, F. *Electrochim. Acta* **1998**, *43*, 2919−2923.
(27) Butler, M. A.; Nasby, R. D.; Quinn, R. K. *Solid State Commun.* **1976**, *19*, 1011−1014.
(28) Amano, F.; Li, D.; Ohtani, B. *Chem. Commun.* **2010**, *46*, 2769−2771.
(29) Berger, S.; Tsuchiya, H.; Ghicov, A.; Schmuki, P. *Appl. Phys. Lett.* **2006**, *88*, 203119−203121.
(30) Amano, F.; Tian, M.; Wu, G.; Ohtani, B.; Chen, A. *ACS Appl. Mater. Interfaces* **2011**, *3*, 4047−4052.
(31) Turner, J. E.; Hendewerk, M.; Somorjai, G. A. *Chem. Phys.Lett.* **1984**, *105*, 581−585.
(32) Kominami, H.; Yabutani, K. -.; Yamamoto, T.; Kera, Y.; Ohtani, B. *J. Mater. Chem.* **2001**, *11*, 3222−3227.
(33) Zheng, H.; Ou, J. Z.; Strano, M. S.; Kaner, R. B.; Mitchell, A.; Kalantar-Zadeh, K. *Adv. Funct. Mater.* **2011**, *21*, 2175−2196.
(34) Xin, G.; Guo, W.; Ma, T. *Appl. Surf. Sci.* **2009**, *256*, 165−169.
(35) Cristino, V.; Caramori, S.; Argazzi, R.; Meda, L.; Marra, G. L.; Bignozzi, C. A. *Langmuir* **2011**, *27*, 7276−7284.